Journal of Energy Storage 139 (2025) 118534

Contents lists available at ScienceDirect

Journal of Energy Storage

journal homepage: www.elsevier.com/locate/est

Research papers

Insights into stability, kinetic, and electrochemical performance of silicon-doped boron carbon nitride as a promising anode material for lithium-ion battery: First-principles calculations

Suresh Sampathkumar [a], Selvarengan Paranthaman [b], Liang-Yin Kuo [a,c,d,e,*]

[a] Department of Chemical Engineering, Ming Chi University of Technology, Taishan, New Taipei City, 24301, Taiwan
[b] Department of Physics and International Research Centre, Kalasalingam Academy of Research and Education (Deemed to be University), Krishnankoil, 626 126, India
[c] Center for Sustainability and Energy Technologies, Chang Gung University, Guishan, Taoyuan City, 33302, Taiwan
[d] Sustainable Electrochemical Energy Development Center, National Taiwan University of Science and Technology, Da'an, Taipei, 106335, Taiwan
[e] Chair for Theoretical Physics VII and Bavarian Center for Battery Technologies, University of Bayreuth, Bayreuth, 95447, Germany

ARTICLE INFO

Keywords:
Carbon-based BCN anode materials
Si-doping
Density functional theory
Fast charging
Storage capacity

ABSTRACT

Two-dimensional boron carbon nitride (BCN) has gained increasing attention for use in lithium-ion batteries (LIBs) due to its unique electronic properties. In this study, the effects of silicon (Si)-doping on the structural, kinetic, and electrochemical properties of BCN are investigated by density functional theory calculations. Minor Si-doping in the BCN lattice (Si-BCN) is found to alter the pore radius, which enhances Li-ion adsorption and diffusion. The Li-ion adsorption energy (E_{ad}) increases from −2.02 eV in pristine BCN to −2.75 eV in Si-BCN nanosheet, indicating stronger Li-ions interaction. This more negative E_{ad} enhances the stability of Li storage sites, while the reduced diffusion barrier (0.13 eV) facilitates efficient Li-ion transport in Si-BCN. Moreover, Si-doping leads to a reduction in the band gap to 1.12 eV, transitioning the material from semi-metallic to metallic behavior and suggesting improved electronic conductivity. The theoretical capacities are 1456 mAh•g^{-1} for pristine BCN and 1428 mAh•g^{-1} for Si-BCN. Although the capacities are comparable, the increased electronic and ionic conductivities of Si-BCN allow for faster de−/lithiation and show the possibility for faster charging/discharging Li-ion cells.

1. Introduction

The demand for energy storage has become increasing day by day due to the rapid growth of renewable energy and technological advancements [1–5]. Among all the energy storage technologies, the rechargeable lithium-ion batteries (LIBs) have been widely used because of their portability, high operating voltage, high energy density, and low maintenance cost [6–8]. LIBs have been applied in portable electronic devices, transportation vehicles, and large-scale grid systems. Despite all these advantages, LIBs are still facing some technological challenges, such as capacity fading, slow charging rates and limited areal capacity in practical applications [3,9]. Commercial LIB electrodes typically operate at areal capacities of ~2–4 mAh•cm^{-2}, which is sufficient for small portable devices but inadequate for high-energy-demand systems such as long-range electric vehicles and stationary grid storage [10]. Achieving higher areal capacity (>10 mAh•cm^{-2}) while maintaining fast ionic/electronic transport, structural stability, and long cycle life remains a major research focus [11,12]. The three main factors determining the Li-ion cell performance is the cathode, electrolyte, and anode. In this work we are focusing on improving the Li-ion diffusion and storage capacity of anode material for LIBs. Currently, graphite has been broadly employed as an anode for LIBs which shows energy stability with low cost and a storage capacity of 372 mAh•g^{-1} [13]. However, due to the technological advances in the last years the potential for further optimization is limited and new materials should be evaluated [14,57].

In contrast to graphite, Li metal anodes offer high theoretical capacity applicable to high-energy applications. However, their practical use is limited by serious safety concerns, primarily due to dendrite formation [8]. Lithium titanate ($Li_4Ti_5O_{12}$, LTO) anodes offer exceptional structural stability, negligible volume change during lithiation/delithiation but their storage capacity is low (~175 mAh•g^{-1}) [15].

* Corresponding author at: Chair for Theoretical Physics VII and Bavarian Center for Battery Technologies, University of Bayreuth, Bayreuth, 95447, Germany.
E-mail address: liang-yin.kuo@uni-bayreuth.de (L.-Y. Kuo).

https://doi.org/10.1016/j.est.2025.118534
Received 5 June 2025; Received in revised form 10 August 2025; Accepted 23 September 2025
Available online 10 October 2025

Recently, $TiNb_2O_7$ (TNO) has attracted much research attention as a promising alternative anode material to LTO, due to its multiple redox reactions (Ti^{4+}/Ti^{3+}, Nb^{5+}/Nb^{4+}, and Nb^{4+}/Nb^{3+}) leading to a higher theoretical capacity (387 mAh•g^{-1}) [16]. However, electronic conductivity and Li-ion diffusion are challenges for TNO anodes. Silicon (Si)-based anodes with even higher theoretical storage capacity (4200 mAh•g^{-1}) than Li metal anodes could be a promising alternative although it must overcome the challenges related to volume expansion and cyclic stability [17]. Yet it is believed that chemical modifications such as Si nanostructures, Si-based composites, surface coatings and electrolyte modifications can provide stability and enhance the electrochemical performances of Si-based anode materials [18]. Apart from these, various carbon (C)-based anode materials including inorganic materials such as graphyne (558 mAh•g^{-1}) [19], graphene (744 mAh•g^{-1}) [8], carbon nanotubes (1000 mAh•g^{-1}) [20], carbon nitride (2092 mAh•g^{-1}) [21] *etc.*, have also been investigated for possible anode materials of LIBs. In our previous study, we have investigated monolayer graphdiyne (GDY) and nitrogen (N)-doped bilayer graphdiyne (BGDY) with AB($\beta 1$) stacking as anode material for LIBs [22]. We found that the N-doping in BGDY improves the Li-ion storage capacity from 744 mAh•g^{-1} (GDY) to 807 mAh•g^{-1}. Moreover, the band gap and volume change are reduced with N-doping, which are helpful for fast-charging and increased mechanical stability during cycling.

Doping carbon-based materials with heteroatoms, particularly boron (B) and N atoms, can effectively alter its electronic properties [23,24]. Recently, the combination of B, C and N led to a ternary $B_xC_yN_z$ system [25,26]. These $B_xC_yN_z$ can be synthesized experimentally by various methods including thermal decomposition [27], chemical vapor deposition [23], doping process [28] *etc.*, and exhibit high surface area with remarkable optical properties. The electronic conductivity of two-dimensional (2D) BCN is in between that of semi-metallic and insulator, for instance graphene (zero band gap) and hexagonal-boron nitride (h-BN: 5.6 eV) [29,30]. Depending on the concentration of B, C and N atoms, the $B_xC_yN_z$ system has different properties such as tunable electronic properties, chemical and thermal stability, catalytic activity, which are not observed in binary 2D systems [31]. Due to this, the $B_xC_yN_z$ system possess new physicochemical properties which leads to various novel applications including LIBs [32]. The presence of B−N and C−N helps in introducing the active sites for electrochemical reactions [29]. Like other 2D materials, $B_xC_yN_z$ systems are suitable active materials for rechargeable batteries. However, their systematic electrochemical evaluation (conductivity, charge-discharge rate, and cyclic stability) is unexplored. Theoretical modeling can thus provide crucial insights into their mechanisms and potential performance, allowing them to judge their suitability for use in LIBs.

Karbhal et al. synthesized a 3D honeycomb boron carbon nitride (HBCN) from boric acid, glucose, and cyanamide and analyzed as an anode material for LIBs [33]. They reported that 3D HBCN exhibits a storage capacity of 652 mAh•g^{-1} in LIBs. Heidari et al. studied pristine and Titanium (Ti)-/Aluminium (Al)-doped B_3CN_4 nanosheets as anodes for magnesium-ion batteries (MIBs) using density functional theory (DFT) calculations [34]. They suggested that Al-B_3CN_4 possesses favorable Mg-ion migration with energy barrier of 0.02 eV and a low open-circuit voltage (OCV) of 0.18 V when applied as anodes in MIB. Rupp et al. studied the doping effects of Si in BC_2N nanotubes and showed that Si-doped BC_2N nanotubes have lower formation energy than Si-doped graphene and h-BN, indicating a benefit for material synthesis [35].

Most of the previous studies focused on BC_xN structures with a B:N ratio of 1 and C-rich such as BC_2N, BC_4N. This is due to the phase separation between graphene and h-BN, which has been observed experimentally [23]. The studies on BCN structures with a B:C:N ratio of 1:1:1 is limited because of the experimental challenges associated with real-time control of elemental ratio [33,36]. Herein, we employed DFT calculations to investigate the atomic structures and energetic properties of pristine and Si-doped BCN with a 1:1:1 ratio of B:C:N. To the best of our knowledge, a comprehensive study of pristine and Si-doped BCN nanosheets with a 1:1:1 ratio as an anode material for LIBs has not yet been conducted. We aim to provide a detailed analysis of its structural stability (atomic and electronic structures), kinetic properties (Li-ion adsorption energy and diffusion) and electrochemical behavior (storage capacity and OCV) by DFT calculations.

2. Computational details

The spin-polarized DFT calculations were performed using the generalized gradient approximation (GGA) [37] implemented in the Vienna *Ab inito* Simulation Package (VASP) [38,39]. The Perdew-Burke-Ernzerhof (PBE) [37] functional was employed to describe the exchange-correlation energy. DFT with Grimme's D3 (DFT-D3) method was utilized to correct van der Waals interactions for pristine and Si-BCN nanosheets [40]. The atomic structures of pristine and Si-BCN nanosheets were optimized by 3 × 3 × 1 supercell with a vacuum of 15 Å along *z*-direction (15.30 × 15.30 Å). Thus, we have 24 B, 24 C, 24 N for pristine BCN nanosheet (totally 72 atoms). In Si-BCN, one Si replaces one B and it has 23 B, 24 C, 24 N and 1 Si atoms respectively. A Monkhorst-Pack *k*-points of 1 × 1 × 1 was employed for geometry optimizations with energy and force convergence criteria of 10^{-5} eV and 0.02 eV $Å^{-1}$. A 3 × 3 × 1 *k*-points mesh was utilized for electronic structure calculations. The energy and force convergence criteria is 10^{-5} eV and 0.02 eV $Å^{-1}$ respectively. The diffusion energy barriers are investigated by calculating minimum energy path using the climbing-image nudged elastic band (CI-NEB) approach [41]. A total of six images were generated between the initial and final states, energy and force convergence criteria is set to 10^{-5} eV and 0.02 eV $Å^{-1}$.

3. Results and discussion

3.1. Atomic and electronic structures of pristine and Si-BCN nanosheets

The optimized structures of pristine and Si-BCN nanosheets are shown in Fig. 1. The 3 × 3 × 1 supercell consists of a total of 72 atoms, *i.e.* 24 B, 24 C, 24 N atoms for pristine and 23 B, 24 C, 24 N, 1 Si atoms for Si-BCN nanosheets respectively. Here, we introduce a single Si dopant in a 3 × 3 × 1 BCN supercell (~1.39 %) to evaluate the fundamental effects of Si substitution. This low doping level avoids interactions between dopants and is consistent with reported experimental results for Si-doping in graphene system [42]. While higher doping levels may further modify the Li adsorption landscape, diffusion kinetics, and structural stability, the present model will serve as a representative case to illustrate the underlying doping-induced mechanisms. Moreover, in this study, Si-BCN refers to the structure with Si-doped at the B site, which shows the lowest formation energy (E_{form}) compared to the structures with Si at the C and N sites, as shown in Table S1. Therefore, the (B-site) Si-BCN is the focus of our analysis. The E_{form} is calculated using the following equation:

$$E_{form} = \frac{E_{BCN/Si-BCN} - (n_B E_B + n_C E_C + n_N E_N + n_{Si} E_{Si})}{N} \quad (1)$$

where E_{BCN} and $E_{Si\text{-}BCN}$ are the total energies of pristine and Si-BCN

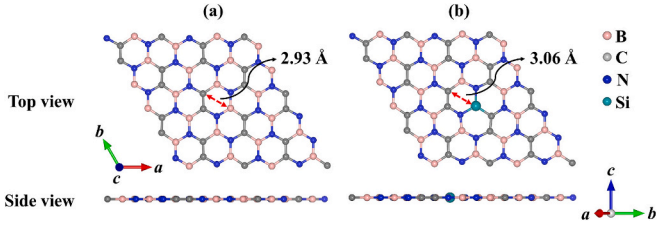

Fig. 1. Optimized geometries of (a) pristine and (b) Si-BCN nanosheets.

nanosheets. E_B, E_C, E_N and E_{Si} are the energies of B, C, N and Si atoms, while n_i (i = B, C, N, Si) represents the number of atoms of type i, and N is the total number of atoms. In Table 1, the calculated E_{form} values are −7.10 and −7.03 eV for pristine and Si-BCN nanosheets. The negative E_{form} values show that both nanosheets are thermodynamically stable. The increase of E_{form} (+0.07 eV) for Si-BCN nanosheet indicates a slight reduction in thermodynamic stability upon substitution of B with Si atom. However, the small energy difference suggests that Si-doping is still energetically favorable under appropriate synthesis conditions.

The lattice parameters a and b of pristine and Si-BCN nanosheets are both 15.30 Å with a vacuum of 15 Å along c-axis. Considering the structural symmetry of the BCN nanosheet, two different hexagons where one with C−C bond and the other without C−C bond are illustrated (Fig. 1). Each hexagon consists of 2 B, 2 C and 2 N atoms and the Si-doped hexagon has 1 B, 2 C, 2 N and 1 Si atoms. The calculated pore radius is 2.93 Å and 3.06 Å for the hexagons of pristine and Si-BCN nanosheets. This is attributed to the larger atomic radius of the Si atom (1.10 Å) than that of the replaced B atom (0.85 Å). Moreover, the doping of Si introduces longer bond lengths in the doped structure (Si−N: 1.653 Å and Si−C: 1.718 Å) compared to those in pristine one (B−N: 1.468 Å and B−C: 1.553 Å). The increased pore radius in Si-BCN nanosheet is helpful for Li-ion adsorption and diffusion. A more detailed discussion is provided in Sections 3.2 and 3.3. However, the bond distances of each element (*i.e.*, B−N, C−N, C−C, and B−C) in Table 1 indicates that a minor Si doping (~1.39 %) does not alter the original configuration.

Fig. 2 (a and b) shows the band structures of pristine and Si-BCN nanosheets. It is found that the band gap reduces from 1.14 eV to 0.02 eV with Si-doping. The semi-metallic behavior of pristine BCN nanosheet is thus changed to metallic behavior for Si-BCN nanosheet. Moreover, the Fermi energy is calculated to increase from −2.56 eV (pristine) to −1.41 eV with Si-doping. A shift of Fermi energy to a higher energy level is also found in the total density of states (TDOS) in Fig. S1. This shift leads to intersect with the conduction band thereby facilitating the charge transfer of Si-BCN. To further understand the contributions of each element, the projected density of states (PDOS) was calculated. The B-2p (pink color) and C-2p (gray color) orbitals exhibit similar features due to overlapping energy region. However, C-2p states show slightly broader features throughout the valence band, indicating more delocalized behavior. The N-2p orbitals (blue color) dominate both the valence and conduction bands, indicating their significant role in the electronic structure. Although the contribution from Si-3p states (dark cyan color) is relatively minor due to the low doping concentration (~1.39 %), it still contributes to orbital hybridization near the Fermi level, potentially enhancing the material's electronic and electrochemical properties. The change in charges is analyzed by the charge density difference (CDD). The CDD plot (Fig. 2c) shows that the Si atom is surrounded by cyan features and the neighboring BCN atoms exhibit more yellow features, indicating electron transfers from the Si dopant to the surrounding atoms. This suggests that Si-doping in BCN increases charge redistribution. Bader charge analysis further supports this finding, showing that the Si dopant donates around 2.65 electrons to the surrounding lattice in Si-BCN, compared to about 1.98 electrons donated by the B atom in pristine BCN. This increased charge donation from Si is consistent with the CDD results and implies improved electronic conductivity in the Si-doped BCN nanosheets.

3.2. Adsorption of Li-ion

The adsorption of Li-ion on the anode surface has a great impact on the storage capacity of the LIBs [3]. After structural optimization, the Li-ion prefers to adsorb at the center of the hexagon formed by C−C bond in the pristine BCN nanosheet (Fig. 3 (a)). However, for the Si-BCN nanosheet, the Li-ion induces a buckling at the Si site and stably adsorbs on the top of the Si atom (Fig. 3 (b)). This is because the Si atom transfers more electron density to the neighboring atoms which makes it an electron-rich site. As a result, the top of Si atom becomes a more favorable adsorption site for the Li-ion. The formation of buckling in Si-BCN offers more diffusion for Li-ion than the pristine BCN. Furthermore, the distance between the Li-ion and the surface is 1.726 Å for the pristine BCN nanosheet and 1.351 Å for the Si-BCN nanosheet. Their adsorption energies (E_{ad}) are calculated using the following equation,

$$E_{ad} = \frac{(E_{nLi+BCN}) - (E_{BCN} + nE_{Li})}{n} \quad (2)$$

where $E_{nLi+BCN}$, E_{BCN} and E_{Li} are the total energy of pristine/Si-BCN with number (n) of adsorbed Li-ions, total energy of pristine/Si-BCN and energy of single Li respectively. A Li atom positioned above B, C, N, and Si atoms, as well as their corresponding bridge and hollow sites were considered to evaluate the E_{ad} at various adsorption sites in pristine and Si-BCN. The calculated E_{ad} values are summarized in Table S2. While the E_{ad} values in Si-BCN tend to be more negative, indicating stronger adsorption, they are not systematically lower than those in pristine ones across all sites. However, Li-ion adsorption at the top of the Si atom shows the most thermodynamically favorable E_{ad} (−2.75 eV) compared to −2.02 eV for pristine BCN at the hollow site. Moreover, the CDD and Barder charge analysis suggest that Si-BCN has more delocalized charge accumulation (yellow surfaces) compared to the pristine (Fig. 3 (c) and (d)), while the charge transfer of 0.74 e and 0.80 e is calculated from Li to pristine and Si-BCN. The result shows that the Si atom in Si-BCN acts as a strong Li binding site with more favorable E_{ad} energy than pristine BCN. Hence, Si-BCN nanosheet is helpful for stabilizing the Li atoms during charge/discharge cycling and reduce Li clustering.

3.3. Diffusion of Li-ion

Diffusion of Li-ions plays an important role in determining the charge-discharge rate of LIBs [43]. The diffusion process is typically characterized by the diffusion energy barrier, with lower energy barriers enabling faster Li-ion transport when the material is used as an anode in LIBs [44,45]. Considering the symmetrical structure of BCN nanosheets in this study, we calculated two possible diffusion pathways between the most stable adsorption sites for the Li-ion within the hexagon channel. These are path I, which diffuses along the channel over B−N bond (x-axis) and path II which crosses the channel over B−C bond (y-axis). The diffusion pathways of Li-ion and its energy profiles for pristine and Si-BCN nanosheets are shown in Fig. 4. In the NEB calculations, six images have been inserted between initial and final position for both pristine and Si-BCN nanosheets respectively. As illustrated in Fig. 4, the lowest diffusion barrier along path I is 0.17 eV and 0.13 eV, and along path II is 0.14 eV and 0.08 eV, for the pristine and Si-BCN nanosheets respectively. This indicates that Li-ion diffusion over the B−N bond (electrophilic nature) is energetically less favorable than over the B−C bond (nucleophilic nature), resulting in a higher energy barrier for path I

Table 1
Bond distance (Å), band gap (E_g), formation energy (E_{form}) and adsorption energy (E_{ad}) of Li-ion (eV) for pristine and Si-BCN.

Anode Materials	Types of Bonds (Å)						E_g (eV)	E_{form} (eV)	E_{ad} (eV)
	B-N	C-N	C-C	B-C	Si-N	Si-C			
Pristine BCN	1.469	1.428	1.401	1.561	–	–	1.14	−7.10	−2.02
Si-BCN	1.468	1.420	1.403	1.553	1.653	1.718	0.02	−7.03	−2.75

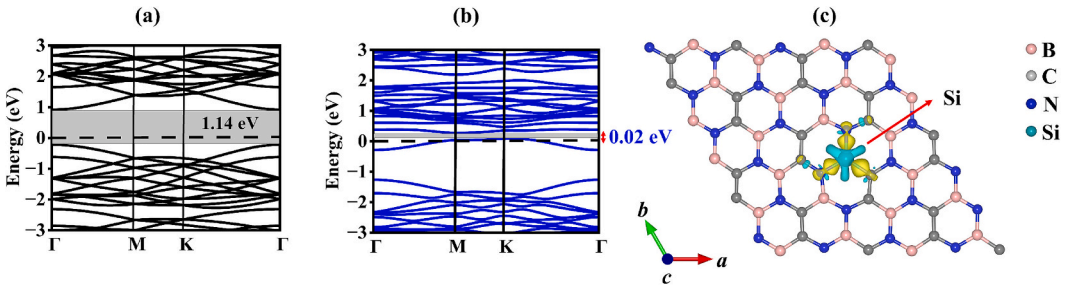

Fig. 2. Band structures of (a) pristine and (b) Si-BCN and (c) charge density difference of Si-BCN (isosurface 0.01 $e/Å^3$, yellow and cyan feature represents electron gain and loss). (For interpretation of the references to color in this figure legend, the reader is referred to the web version of this article.)

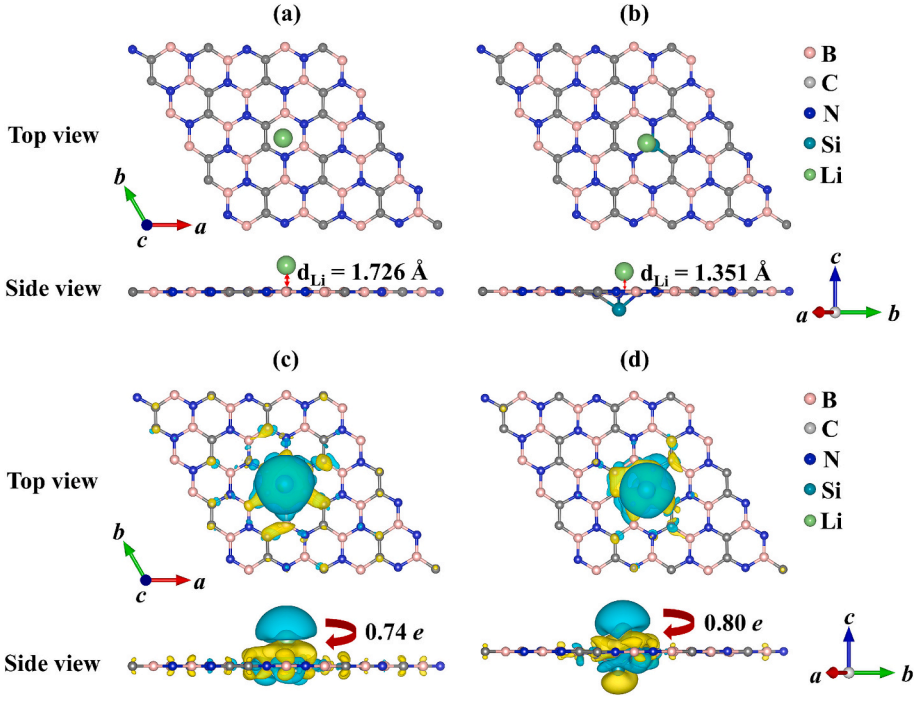

Fig. 3. Optimized geometries and their corresponding CDD and Bader charge analyses induced by a single Li-ion adsorption on pristine (a, c) and Si-BCN (b, d).

than path II. In Si-BCN, a lower energy barrier toward the final state (corresponding to the Si-doping site) is observed in the NEB calculation, particularly along path I. This could be due to the buckled geometry in the Si-BCN framework (see Fig. 3b), which enables local structural relaxation and reduces steric hindrance as Li-ion migrates across the surface. This buckling facilitates an energetically downhill diffusion path, minimizing energy barriers beyond the initial step (Fig. 4c). Moreover, the CDD and Barder charge analyses in Figs. 3 (c) and (d) show increased delocalized charge accumulation (yellow surfaces) and charge transfer in Si-BCN. These findings highlight the key role of Si dopants in modulating the diffusion landscape and enhancing Li-ion kinetics in Si-BCN. However, in both pathways, the Si-BCN nanosheet shows lower diffusion energy barriers than the pristine one, enabling fast ion transport. Notably, the calculated diffusion barriers for pristine and Si-BCN nanosheets are both lower than the diffusion barrier of commercial graphite anode 0.45–1.2 eV [46]. Table 2 lists a comparison of the diffusion barriers with the current study. These findings reveal that the diffusion barrier for Li-ion on pristine and Si-BCN nanosheets is much smaller compared to some previously reported materials, indicating fast Li-ion migration in these systems.

3.4. Storage capacity and open-circuit voltage

The practical application of designed anode material mainly depends on two key factors: storage capacity and open-circuit voltage (OCV). In this study, the storage capacity and OCV are calculated by using the following equation,

$$\text{capacity} = \frac{n\text{F}}{3600\text{M}_{\text{BCN}}} \tag{3}$$

$$\text{OCV} = \frac{E_{\text{BCN}} - E_{n\text{Li+BCN}} + nE_{\text{Li-bulk}}}{ne} \tag{4}$$

where n is the number of adsorbed Li-ions, F is the faraday constant (96,500 mAh), the number of 3600 is the number of Coulombs in 1 Ampere-hour, M_{BCN} is the molar mass of the pristine BCN (884 g•mol^{-1})/Si-BCN (901 g•mol^{-1}). $E_{Li\text{-bulk}}$ is the energy of bulk body-centered cubic (bcc) Li. The Li-ions are successively put at favorable adsorption sites on both sides of the BCN nanosheets and optimized to calculate the storage capacity and OCV. The results show that the pristine and Si-BCN nanosheets can store up to 48 Li-ions with the compositions of Li_2BCN and $Li_2B_{0.96}Si_{0.04}CN$, respectively. The corresponding optimized structures are shown in Fig. 5. There are two main factors influencing the Li-ion adsorption on the anode materials, (i) the

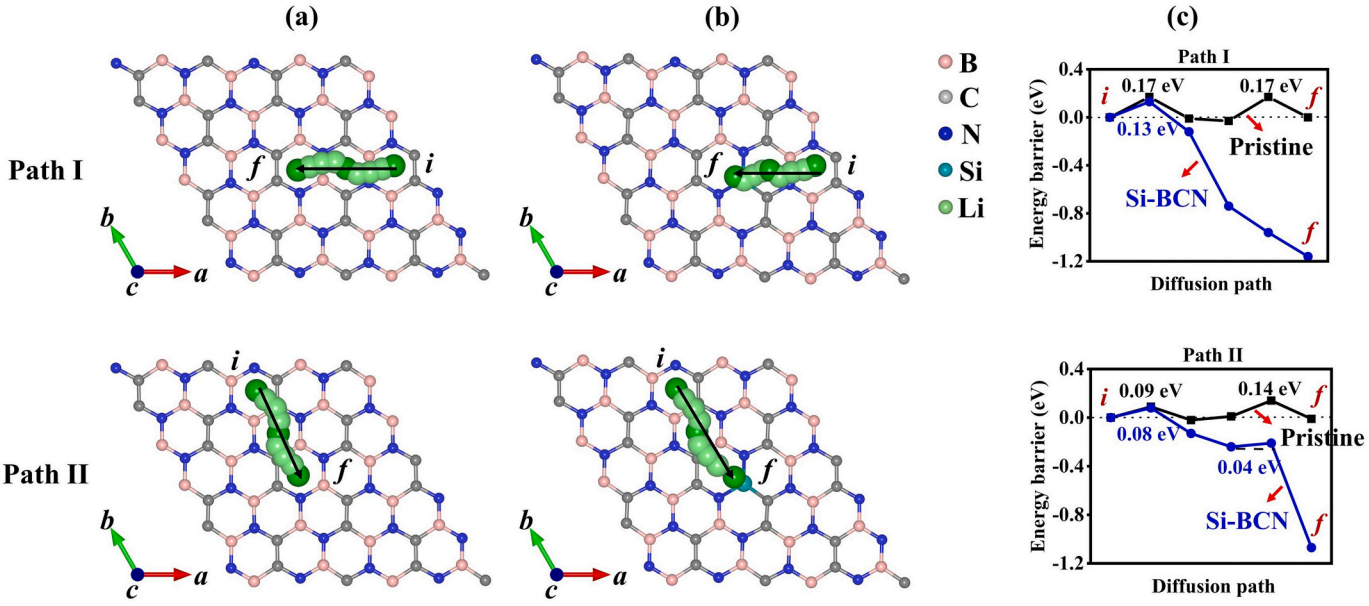

Fig. 4. Two different diffusion pathways of Li-ion on (a) pristine and (b) Si-BCN nanosheets and (c) corresponding energy profiles plotted through CI-NEB calculations (*i*: initial, *f*: final).

Table 2
Comparision of some of the previously reported anode materials with current work.

Anode Materials	Diffusion barrier (eV)	Storage capacity ($mAh•g^{-1}$)	OCV (V)	Reference
Graphite	0.45–1.20	372	0.25	[46,50]
Graphdiyne	0.61	744	0.68	[22]
Graphyne	0.97	558	0.84	[51]
Silicene	1.33	716	0.42	[52]
BC_3N_3	1.13	–	–	[53]
SiC_3N_3	0.73	253	0.48	[54]
penta-Graphene	0.17	1489	0.55	[55]
penta-BCN	0.14	2183	0.46	[56]
penta-SiCN	0.11	1486	0.97	[43]
pristine-BCN	0.17	1456	0.64	Current work
Si-BCN	0.13	1428	0.64	Current work

repulsive forces between neighboring Li-ions, (ii) changes in the adsorption structure [47]. The calculated average Li−Li bond distance between the neighboring Li-ions shows that weaker interatomic repulsion occurs in Si-BCN (3.15 Å) compared to the pristine BCN (2.85 Å). The longer average Li-Li spacing in Si-BCN arises due to the structural distortion and local buckling introduced by Si-doping, which slightly expands the lattice and modifies the spatial arrangement of favorable Li adsorption sites. This increased separation reflects a weaker interatomic repulsion between Li ions in Si-BCN, consistent with the basic electrostatic principle that repulsion decreases with increasing distance. In contrast, the shorter average Li-Li distance in pristine BCN (2.85 Å) indicates a more compact Li arrangement and stronger repulsion, which may contribute to a higher degree of Li-Li interaction and possible clustering effects. Furthermore, symmetric and asymmetric interlayer spacing is observed in pristine and Si-BCN upon Li-ion adsorption. The interlayer spacing is almost equal in both sides for pristine BCN (1.92 & 1.96 Å) and it is unequal in Si-BCN nanosheet (1.92 & 2.04 Å). The weaker ionic repulsion between the Li-ions in Si-BCN maximizes their spatial separation resulting in a distorted adsorption geometry and increased interlayer spacing (Fig. 5b). The larger interlayer spacing could promote faster Li-ion diffusion. This effect in Si-doped graphene compared to pristine one has also been recently reported by Liu et al. [42]. The E_{ad} for pristine and Si-BCN nanosheets with maximum amount of Li-ion adsorbed are −1.44 eV and −1.52 eV respectively. The more negative E_{ad} value and decreased ionic repulsion in the Si-BCN nanosheet could improve the stabilization of Li atoms during charge/discharge cycling. Although Si-doping improves Li stabilization,

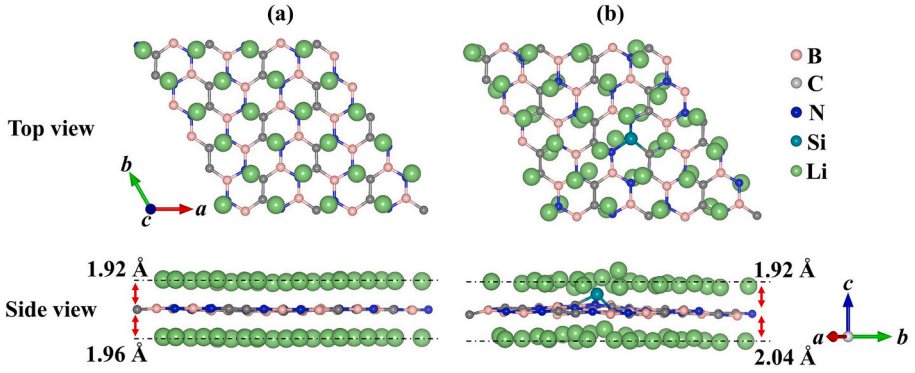

Fig. 5. Optimized structures of the maximum number of Li atoms (48 atoms) adsorbed on (a) pristine and (b) Si-BCN nanosheets, resulting in Li_2BCN and $Li_2B_{0.96}Si_{0.04}CN$ compositions.

increasing the Si-doping level (*i.e.* >1.39 %) may be required to effectively mitigate Li clustering [22,48,49]. The calculated maximum storage capacities are 1456 mAh•g^{-1} and 1428 mAh•g^{-1} for pristine and Si-BCN nanosheets. The above values are almost four times than that of commercial graphite anode 372 mAh•g^{-1} for LIBs [50]. The calculated storage capacity in this study and other works are listed in Table 2.

Furthermore, the calculated average OCV is 0.64 V for both pristine and Si-BCN nanosheets within the range of 1.25–0.03 V. The above OCV value is comparable to our recently reported OCV values of graphdiyne (0.68 V) [22]. The resulting low average OCV helps prevent the clustering of Li-ions during the operation of LIBs. Thus, pristine and Si-BCN nanosheets with their low average OCV and high Li storage capacity hold promise as a high-performance anode for LIBs. Table 2 illustrates the OCV in this study and other works.

4. Conclusion

Our simulations show that the electronic and ionic properties of a BCN nanosheet can be tailored through Si-doping and thus improve its electrochemical properties. While the structure of BCN is stable with a Si-doping of 1.39 %, it increases its pore radius and reduces the band gap from 1.14 eV (pristine) to 0.02 eV, effectively transforming BCN from a semi-metallic to a metallic system. The increased pore size enhances both Li-ion adsorption and diffusion. Specifically, the Li-ion adsorption energy improves from −2.02 eV in pristine BCN to −2.75 eV in Si-BCN nanosheet. Moreover, the Li-ion diffusion barrier is reduced from 0.17 eV to 0.13 eV, indicating improved ionic mobility. Finally, pristine and Si-BCN nanosheets show comparable theoretical capacities, 1456 mAh•g^{-1} and 1428 mAh•g^{-1}, respectively. However, Si-doping improves structural integrity as well as electronic and ionic conductivities, enabling a faster charging/discharging process as required in anodes for high-performance LIBs. This study offers a comprehensive analysis of the structural and kinetic properties of BCN nanosheets, providing valuable insights for experimental production.

CRediT authorship contribution statement

Suresh Sampathkumar: Writing – review & editing, Writing – original draft, Methodology, Investigation, Formal analysis, Data curation, Conceptualization. **Selvarengan Paranthaman:** Writing – review & editing, Supervision, Conceptualization. **Liang-Yin Kuo:** Writing – review & editing, Supervision, Resources, Methodology, Investigation, Funding acquisition, Formal analysis, Data curation, Conceptualization.

Declaration of competing interest

The authors declare that they have no known competing financial interests or personal relationships that could have appeared to influence the work reported in this paper.

Acknowledgement

The authors S. S and L-Y. K gratefully acknowledge financial support from the Ministry of Science and Technology, Taiwan (Project No: NSTC113-2221-E-131-034). Computing resources were generously provided by the National Center for High-performance Computing (NCHC) on Taiwania 3 in Hsinchu, Taiwan.

Appendix A. Supplementary data

Supplementary data to this article can be found online at https://doi.org/10.1016/j.est.2025.118534.

Data availability

Data will be made available on request.

References

[1] H. Chen, T.N. Cong, W. Yang, C. Tan, Y. Li, Y. Ding, Progress in electrical energy storage system: a critical review, Prog. Nat. Sci. 19 (2009) 291–312.
[2] Y. Yang, S. Bremner, C. Menictas, M. Kay, Battery energy storage system size determination in renewable energy systems: a review, Renew. Sust. Energ. Rev. 91 (2018) 109–125.
[3] K. Fan, Y.H. Tsang, H. Huang, Computational design of promising 2D electrode materials for Li-ion and Li–S battery applications, MRE 3 (2023) 100213.
[4] K.-C. Lee, J.-H. Huang, W.K. Pang, K.-S. Wang, S.-C. Hsu, H.C. Weng, T.-Y. Liu, Development of asphaltene-derived hierarchically activated carbon and carbon-coated $Li_4Ti_5O_{12}$ for high-performance lithium-ion capacitors, J. Energy Storage 119 (2025) 116325.
[5] K.-C. Lee, J.-H. Huang, Y.-J. Wu, K.-S. Wang, E.-C. Cho, S.-C. Hsu, T.-Y. Liu, Crystal structure-controlled synthesis of $NiMoO_4$/NiO hierarchical microspheres for high-performance supercapacitors and photocatalysts, J. Energy Storage 97 (2024) 112639.
[6] M. Wakihara, Recent developments in lithium ion batteries, Mater. Sci. Eng. R. Rep. 33 (2001) 109–134.
[7] P. Roy, S.K. Srivastava, Nanostructured anode materials for lithium ion batteries, J. Mater. Chem. A 3 (2015) 2454–2484.
[8] P.U. Nzereogu, A.D. Omah, F.I. Ezema, E.I. Iwuoha, A.C. Nwanya, Anode materials for lithium-ion batteries: a review, Appl. Surf. Sci. Adv. 9 (2022) 100233.
[9] S. Zhou, P. Huang, T. Xiong, F. Yang, H. Yang, Y. Huang, D. Li, J. Deng, M. S. Balogun, Sub-thick electrodes with enhanced transport kinetics via in situ epitaxial heterogeneous interfaces for high areal-capacity lithium ion batteries, Small 17 (2021) 2100778.
[10] H. Yang, T. Xiong, Z. Zhu, R. Xiao, X. Yao, Y. Huang, M.S. Balogun, Deciphering the lithium storage chemistry in flexible carbon fiber-based self-supportive electrodes, Carbon Energy 4 (2022) 820–832.
[11] G. Li, T. Ouyang, T. Xiong, Z. Jiang, D. Adekoya, Y. Wu, Y. Huang, M.S. Balogun, All-carbon-frameworks enabled thick electrode with exceptional high-areal-capacity for Li-ion storage, Carbon 174 (2021) 1–9.
[12] Z. Khanam, T. Xiong, F. Yang, H. Su, L. Luo, J. Li, M. Koroma, B. Zhou, M. Mushtaq, Y. Huang, T. Ouyang, M.S. Balogun, Endogenous interfacial Mo−C/N−Mo-S bonding regulates the active Mo sites for maximized Li^+ storage areal capacity, Small 20 (2024) 2311773.
[13] H. Zhang, Y. Yang, D. Ren, L. Wang, X. He, Graphite as anode materials: Fundamental mechanism, recent progress and advances, Energy Storage Mater. 36 (2021) 147–170.
[14] J. Zhuang, X. Xu, G. Peleckis, W. Hao, S.X. Dou, Y. Du, Silicene: a promising anode for lithium-ion batteries, Adv. Mater. 29 (2017) 1606716.
[15] A. Kazemi, R. Mostaani, M.K. Ravari, M. Ghorbanzadeh, M. Yavarinasab, J. Enferadi, Z. Chen, N. Iqbal, Y. Xiang, W. Liu, A. Davoodi, Enhancing high rate performance of lithium titanium oxide (LTO) anodes: a comprehensive review, J. Power Sources 630 (2025) 236051.
[16] Y.-S. Hsiao, L.-Y. Chang, C.-W. Hu, C.-Z. Lu, N.-J. Wu, Y.-L. Chen, T.-H. Hsieh, J.-H. Huang, S.-C. Hsu, H.-C. Weng, C.-P. Chen, Cr^{3+}-doped $TiNb_2O_7$ as an advanced anode material for high-performance lithium-ion batteries, Appl. Surf. Sci. 614 (2023) 156155.
[17] L. Wang, J. Yu, S. Li, F. Xi, W. Ma, K. Wei, J. Lu, Z. Tong, B. Liu, B. Luo, Recent advances in interface engineering of silicon anodes for enhanced lithium-ion battery performance, Energy Storage Mater. 66 (2024) 103243.
[18] Y.-S. Hsiao, J.-H. Huang, T.-H. Hsieh, L.-Y. Weng, S.-W. Liao, Y.-C. Yen, W.K. Pang, S.-C. Hsu, H.C. Weng, Y.-C. Huang, Spray-dried nanoarchitectonics of SiO_x/C composite as a high-performance anode material for lithium-ion batteries, J. Taiwan Inst. Chem. Eng. (2025) 106243. In press.
[19] C. Sun, D.J. Searles, Lithium storage on graphdiyne predicted by DFT calculations, J. Phys. Chem. C 116 (2012) 26222–26226.
[20] S. Ullah, P.A. Denis, F. Sato, Beryllium doped graphene as an efficient anode material for lithium-ion batteries with significantly huge capacity: a DFT study, Appl. Mater. Today 9 (2017) 333–340.
[21] A. Ghosh, S. Mandal, P. Sarkar, 2D homogeneous holey carbon nitride: an efficient anode material for Li-ion batteries with ultrahigh capacity, ChemPhysChem 23 (2022) e202200182.
[22] M. Tam Le, L.-Y. Kuo, Y.-Z. Wu, M. Ihrig, N.N.T. Pham, Enabling fast-charging and high specific capacity of Li-ion batteries with nitrogen-doped bilayer graphdiyne: a first-principles study, Batteries Supercaps 8 (2025) e202400352.
[23] L. Ci, L. Song, C. Jin, D. Jariwala, D. Wu, Y. Li, A. Srivastava, Z.F. Wang, K. Storr, L. Balicas, Atomic layers of hybridized boron nitride and graphene domains, Nat. Mater. 9 (2010) 430–435.
[24] L. Caputo, V.H. Nguyen, J.C. Charlier, First-principles study of the structural and electronic properties of BN-ring doped graphene, Phys. Rev. Mater. 6 (2022) 114001.
[25] L. Cheng, J. Meng, X. Pan, Y. Lu, X. Zhang, M. Gao, Z. Yin, D. Wang, Y. Wang, J. You, J. Zhang, E. Xie, Two-dimensional hexagonal boron–carbon–nitrogen atomic layers, Nanoscale 11 (2019) 10454–10462.
[26] N.R. Abdullah, H.O. Rashid, C.-S. Tang, A. Manolescu, V. Gudmundsson, Modeling electronic, mechanical, optical and thermal properties of graphene-like BC_6N materials: Role of prominent BN-bonds, Phys. Lett. A 384 (2020) 126807.
[27] F. Leardini, L. Massimi, E. Flores-Cuevas, J.F. Fernández, J.R. Ares, M.G. Betti, C. Mariani, Synthesis of ternary borocarbonitrides by high temperature pyrolysis of ethane 1, 2-diamineborane, Materials 8 (2015) 5974–5985.
[28] C. Zhao, Z. Xu, H. Wang, J. Wei, W. Wang, X. Bai, E. Wang, Carbon-doped boron nitride nanosheets with ferromagnetism above room temperature, Adv. Funct. Mater. 24 (2014) 5985–5992.

[29] S.A. Thomas, J. Cherusseri, M.R. Pallavolu, D.N. Rajendran, D. Kumar, Boron carbon nitride (BCN): an emerging two-dimensional material for rechargeable batteries, ENFL 38 (2024) 13704–13721.
[30] L. Song, L. Ci, H. Lu, P.B. Sorokin, C. Jin, J. Ni, A.G. Kvashnin, D.G. Kvashnin, J. Lou, B.I. Yakobson, P.M. Ajayan, Large scale growth and characterization of atomic hexagonal boron nitride layers, Nano Lett. 10 (2010) 3209–3215.
[31] A. Rubio, Nanoscale patchworks, Nat. Mater. 9 (2010) 379–380.
[32] S. Tazekritt, M. Gallouze, A. Kellou, DFT study of energetics and optoelectronics properties of B, C, and N binary and ternary honeycomb structures, J. Appl. Phys. 135 (2024) 094302.
[33] I. Karbhal, V. Chaturvedi, A. Patrike, P. Yadav, M.V. Shelke, Honeycomb boron carbon nitride as high-performance anode material for Li-ion batteries, ChemNanoMat 8 (2022) e202200056.
[34] S. Heidari, M.D. Esrafili, J.J. Sardroodi, Pristine and Ti- or Al-doped B_3CN_4 nanosheets as efficient anodes for Mg-ion batteries: A DFT study, J. Energy Storage 93 (2024) 112109.
[35] C.J. Rupp, J. Rossato, R.J. Baierle, First principles study of Si-doped BC_2N nanotubes, J. Chem. Phys. 130 (2009).
[36] R.B. Kaner, J. Kouvetakis, C.E. Warble, M.L. Sattler, N. Bartlett, Boron-carbon-nitrogen materials of graphite-like structure, Mater. Res. Bull. 22 (1987) 399–404.
[37] J.P. Perdew, K. Burke, M. Ernzerhof, Generalized gradient approximation made simple, Phys. Rev. Lett. 77 (1996) 3865.
[38] G. Kresse, J. Furthmüller, Efficiency of ab-initio total energy calculations for metals and semiconductors using a plane-wave basis set, Comput. Mater. Sci. 6 (1996) 15–50.
[39] G. Kresse, J. Furthmüller, Efficient iterative schemes for ab initio total-energy calculations using a plane-wave basis set, Phys. Rev. B 54 (1996) 11169.
[40] S. Grimme, J. Antony, S. Ehrlich, H. Krieg, A consistent and accurate ab initio parametrization of density functional dispersion correction (DFT-D) for the 94 elements H-Pu, J. Chem. Phys. 132 (2010).
[41] G. Henkelman, B.P. Uberuaga, H. Jónsson, A climbing image nudged elastic band method for finding saddle points and minimum energy paths, J. Chem. Phys. 113 (2000) 9901–9904.
[42] H. Liu, W. Yang, S. Che, Y. Li, C. Xu, X. Wang, G. Ma, G. Huang, Y. Li, Silicon doped graphene as high cycle performance anode for lithium-ion batteries, Carbon 196 (2022) 633–638.
[43] X.-J. Ye, X.-H. Wang, H.-B. Cao, Z. Lu, C.-S. Liu, Penta-SiCN monolayer as a well-balanced performance anode material for Li-ion batteries, Phys. Chem. Chem. Phys. 25 (2023) 29224–29232.
[44] D. Adekoya, S. Zhang, M. Hankel, Boosting reversible lithium storage in two-dimensional C3N4 by achieving suitable adsorption energy via Si doping, Carbon 176 (2021) 480–487.
[45] H.-H. Hsia, G.-H. Li, Y.-X. Lan, R. Kunwar, L.-Y. Kuo, J.-M. Yeh, W.-R. Liu, Experimental and theoretical calculations of fluorinated few-layer graphene/epoxy composite coatings for anticorrosion applications, Carbon 217 (2024) 118604.
[46] P. Ganesh, J. Kim, C. Park, M. Yoon, F.A. Reboredo, P.R.C. Kent, Binding and diffusion of lithium in graphite: quantum Monte Carlo benchmarks and validation of van der Waals density functional methods, J. Chem. Theory Comput. 10 (2014) 5318–5323.
[47] B. Ipaves, J.F. Justo, L.V.C. Assali, Aluminum functionalized few-layer silicene as anode material for alkali metal ion batteries, Mol. Syst. Des. Eng. 8 (2023) 379–387.
[48] H.J. Hwang, J. Koo, M. Park, N. Park, Y. Kwon, H. Lee, Multilayer graphynes for lithium ion battery anode, J. Phys. Chem. C 117 (2013) 6919–6923.
[49] Q. Zhang, C. Tang, L. Fu, The first-principle study on the performance of biaxial strained graphdiyne as the Li-ion battery anode, Appl. Surf. Sci. 497 (2019) 143723.
[50] J.M. Tarascon, M. Armand, Issues and challenges facing rechargeable lithium batteries, Nature 414 (2001) 359–367.
[51] M. Lemaalem, N. Khossossi, G. Bouder, P. Dey, P. Carbonnière, Graphyne-based membrane as a promising candidate for Li-battery electrodes protection: Insight from atomistic simulations, J. Power Sources 581 (2023) 233482.
[52] M. Liu, Z. Cheng, X. Zhang, Y. Li, L. Jin, C. Liu, X. Dai, Y. Liu, X. Wang, G. Liu, Two-dimensional dumbbell silicene as a promising anode material for (Li/Na/K)-ion batteries, Chin. Phys. B 32 (2023) 096303.
[53] X. Xia, H. Yin, Y. Zhang, S. Huang, Boron-doped g-CN monolayer as a promising anode for Na/K-ion batteries, Surf. Interfaces 36 (2023) 102479.
[54] X. Xia, J. Wu, X. Cai, B. Liu, Z. Wang, Y. Zhang, S. Huang, SiC_3N_3 monolayer as a universal anode for alkali metal-ion batteries, Dalton Trans. 52 (2023) 10895–10904.
[55] B. Xiao, Y.-c. Li, X.-f. Yu, J.-b. Cheng, Penta-graphene: a promising anode material as the Li/Na-ion battery with both extremely high theoretical capacity and fast charge/discharge rate, ACS Appl. Mater. Interfaces 8 (2016) 35342–35352.
[56] L. Chen, M. Yang, F. Kong, W. Du, J. Guo, H. Shu, Penta-BCN monolayer with high specific capacity and mobility as a compelling anode material for rechargeable batteries, Phys. Chem. Chem. Phys. 23 (2021) 17693–17702.
[57] J.-H. Cheng, Y.-H. Chen, Y.-S. Yeh, S. Hy, L.-Y. Kuo, B.-J. Hwang, Electrochim. Acta 197 (2016) 146–151.